JOURNAL OF SOLID STATE CHEMISTRY 93, 378–394 (1991)

Electron Nuclear Double Resonance Study of $LaMgAl_{11}O_{19}:Ti^{3+}$

D. GOURIER* AND D. VIVIEN

Chimie Appliquée de l'État Solide, URA 302 CNRS, 11 Rue Pierre et Marie Curie, 75231 Paris Cedex 05, France

AND C. WYON

LETI IRDI-CEA, Centre d'Études Nucléaires de Grenoble, 85X-38041 Grenoble Cedex, France

Received January 14, 1991

$LaMgAl_{11}O_{19}:Ti^{3+}$ is studied by electron nuclear double resonance (ENDOR) spectroscopy. ^{27}Al ENDOR of Ti^{3+} in octahedral (2*a*) sites shows a strong covalent interaction between the Ti^{3+} ion and Al^{3+} ions in the nearest octahedral (12*k*) sites. The EPR line of titanium in the (2*a*) site exhibits a significant strain broadening. ENDOR experiments show that this effect is due to a crystal field disorder, which probably results from a statistical occupancy of the neighboring tetrahedral (4*f*) site by Mg^{2+} and Al^{3+} ions. This work also provides evidence that hydrogen atoms diffuse in the spinel blocks during crystal growth. ENDOR of titanium in the octahedral (12*k*) site shows the existence of a neighboring proton trapped between the two oxygen ions bridging two (12*k*) sites. Our results suggest that this proton belongs to a $Ti^{3+}(H^+,Mg^{2+})$ defect cluster and that it compensates the lack of positive charge due to an antisite defect, which is a Mg^{2+} ion in the (12*k*) aluminum site. © 1991 Academic Press, Inc.

I. Introduction

Titanium-doped sapphire has been in recent years the major innovation in the field of solid state tunable laser materials (*1*, *2*). Several firms are now selling titanium sapphire lasers which can be pumped by lamps or by another laser (argon–ion or frequency-doubled Nd : YAG lasers). Among the virtues of this material are a broad tunability (680–1000 nm) and the lack of ground or excited state absorption of the laser emission. Due to the success of titanium sapphire, other titanium-activated matrices have been studied recently, among which are $MgAl_2O_4$ (*3*), $YAlO_3$ (*4*), $Y_3Al_5O_{12}$ (*5*), and $BeAl_2O_4$ (*6*, *7*). Laser action has been observed for $YAlO_3$ and $BeAl_2O_4$.

Recently, several groups have manifested an interest in the $LaMgAl_{11}O_{19}$ (LMA) matrix, which can be grown in the form of large single crystals (*8*). This material belongs to the hexagonal magnetoplumbite ($PbFe_{12}O_{19}$)-type structure (space group $P6_3/mmc$). The ideal unit cell is made of spinel-like blocks separated by mirror planes (Fig. 1). The spinel blocks contain most of the Al^{3+} and Mg^{2+} cations distributed among octahedral and tetrahedral sites, the Mg^{2+} ions being mainly located in the (4*f*) tetrahedra (*9*). The stoichiometric composition $LaMgAl_{11}O_{19}$ corresponds to 50% of the (4*f*) sites being occupied by Mg^{2+} ions. The La^{3+} cations (in 12-fold coordina-

* To whom correspondence should be addressed.

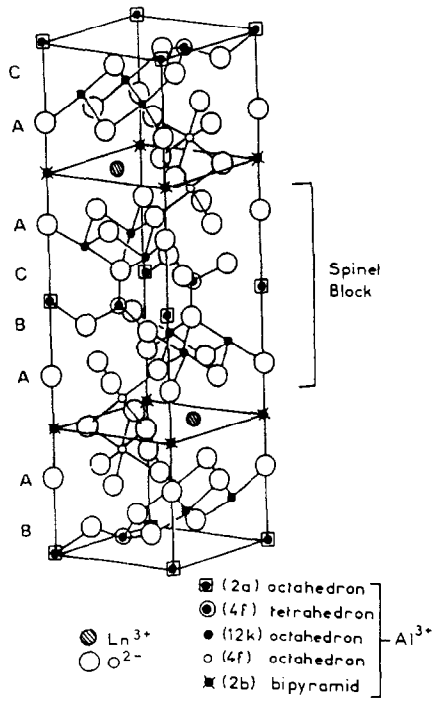

FIG. 1. The unit cell of $LaMgAl_{11}O_{19}$ with magnetoplumbite structure.

tion) and other Al^{3+} ions (in a trigonal bipyramidal site) are located in the mirror planes (Table I). Thus the LMA matrix offers the possibility of three kinds of substitutions:

—La^{3+} by other lanthanide ions leading to a powerful laser (LNA = $La_{1-x}Nd_xMgAl_{11}O_{19}$) which gives stimulated emission at 1.054 and 1.082 μm) (*10*).

—Mg^{2+} by divalent transition metal ions leading to potential tunable laser materials (e.g., $LaMg_{1-x}Ni_xAl_{11}O_{19}$, with emission around 1.1 μm) (*11*).

—Al^{3+} by trivalent transition metal ions leading to potential vibronic lasers such as $LaMgAl_{11-x}Cr_xO_{19}$, a red to near infrared laser (*12*) that can substitute for alexandrite $BeAl_2O_4:Cr^{3+}$. The partial substitution of Al^{3+} ions by Ti^{3+} in the LMA matrix could give an alternative to titanium-doped sapphire (*8, 13*).

The LMA matrix offers three kinds of octahedral sites for titanium ions, namely (2*a*), (4*f*), and (12*k*) sites, with D_{3d}, C_{3v}, and C_s symmetries, respectively (Table I and Fig. 1). This implies a high titanium solubility, up to one atom by formula unit (*14*). Therefore we expect an increased tunability range with respect to the α-alumina matrix. We recently studied by EPR the distribution of Ti^{3+} among the different octahedral sites (*15*). It was shown that a low doping level, 86% of Ti^{3+} occupies the octahedral (2*a*) site (also referred to as site 3) (Fig. 1). The other fraction of Ti^{3+} occupies the octahedral sites (12*k*) (12% occupancy) and (4*f*) (2% occupancy), also referred to as sites 2 and 1, respectively. The *g*-tensor of Ti^{3+} in the (12*k*) site (site 2) was interpreted as resulting from a nonidentified defect in a neighboring (12*k*) site. Part of the titanium also enters the lattice in the (4+) oxidation state. At low titanium content, Ti^{4+} is found only in the (2*a*) site (*15*).

This material also exhibits a broad fluorescence at 775 nm (*8, 15*) typical of a $^2E \rightarrow {}^2T_2$ transition of Ti^{3+} ions in the octahedral site (*1–5*). The fluorescence lifetime was found to be ≈ 4 μs at room temperature. The EPR results led us to deduce that the fluorescence originates from Ti^{3+} in the most populated (2*a*) sites.

The polarized optical absorption (OA) spectra of LMA : Ti exhibit a more complex structure (*8, 16*). When the electric field vector **E** of the polarized light is perpendicular to the *c*-axis, the OA spectrum shows only the $^2T_2 \rightarrow {}^2E$ transition of Ti^{3+} in octahedral (2*a*) sites at $\approx$580 nm. However, for $\mathbf{E} \| \mathbf{c}$, two bands at $\approx$730 and $\approx$980 nm appear in addition to the 580-nm band of Ti^{3+}. Similar infrared bands, which occur in the expected tunability range of the laser emission, have also been found in other titanium-activated matrices (*4*). These bands lying in the wavelength range of the Ti^{3+} fluorescence in LMA can impede laser applications of the material (*17*). Various attempts to suppress

TABLE I

EPR PARAMETERS AND SITE SYMMETRIES IN $LaMgAl_{11}O_{19}$:Ti

Atoms	g factors	Direction of g axes	Localization	Coordination	Geometry	Symmetry
Al^{3+}, Ti^{3+} site 1	$g_{\parallel} = 1.999$ $g_{\perp} = 1.958$	c	$4f$	6	Distorted octahedron	C_{3v}
Al^{3+}, Ti^{3+} site 2	$g_y = 1.975$ $g_x = 1.926$ $g_z = 1.929$	a c	$12k$	6	Distorted octahedron	C_s
Al^{3+}, Ti^{3+} site 3	$g_{\parallel} = 1.9623$ $g_{\perp} = 1.7962$	c	$2a$	6	Regular octahedron	D_{3d}
Al^{3+}, Mg^{2+}			$4f$	4	Tetrahedron	C_{3v}
Al^{3+}			$2b$ (ideal) $4e$ (real)	5 (ideal) 4 (real)	Trigonal bipyramid tetrahedron	D_{3h} C_{3v}
La^{3+}			$2d$ and $(6h)$	12 and (8)		D_{3h} and (C_{2v})

these parasite absorption bands have recently been described (*16*). The band peaking at 730 nm was ascribed to an intervalence charge transfer (IVCT) transition of coupled Ti^{3+}–Ti^{4+} pairs, and the band at 960 nm was tentatively interpreted as a Ti^{2+}–Ti^{3+} intervalence charge transfer (*16*). The polarization of these bands implies that in both cases, the titanium ions of the pair are located in adjacent face-sharing octahedral ($4f$) sites.

It thus appeared that further spectroscopic investigations were needed to understand the complex behavior of Ti^{3+} in the LMA matrix. The present paper reports the study of LMA:Ti using electron nuclear double resonance (ENDOR) spectroscopy (*18*). This technique is complementary to EPR spectroscopy, with the advantage of a much higher resolution without significant loss of sensitivity. In an ENDOR experiment, we detect NMR transitions of ions with nonzero nuclear spins surrounding the paramagnetic ion. With this technique, weak titanium–cation interactions undetectable by EPR can be measured. The nuclei which can be studied by ENDOR in LMA are ^{27}Al ($I = 5/2$), ^{139}La ($I = 7/2$), and also possible impurities such as hydrogen. Indeed, it is known that protons can diffuse in crystals during crystal growth, as, for instance, in the case of spinel $MgAl_2O_4$ (*19*).

The initial purpose of this work was to obtain information concerning Ti^{3+} in ($4f$) sites, which is presumably responsible for the two infrared parasite absorption bands. Our efforts were not successful because the titanium occupancy of this site was too low to give detectable ENDOR lines, so that we could only study the ENDOR of Ti^{3+} in the most populated ($2a$) and ($12k$) sites. However, we obtained interesting results concerning these two sites. In particular, we could show that Ti^{3+} in the ($2a$) site (site 3) exhibits a strong covalent interaction with Al^{3+} in ($12k$) sites and no interaction with Al^{3+} in the other neighboring ($4f$) sites. Moreover we showed that Ti^{3+} in the ($12k$) site (site 2) is adjacent to a defect in a neighboring ($12k$) site.

II. Experimental

Single crystals of $LaMgAl_{11-x}Ti_xO_{19}$ ($x = 0.1$) were grown at LETI by one of the authors (C.W.) through the Czochralski

method using a radio-frequency (rf)-heated iridium crucible under nitrogen atmosphere (gas flow: 21 liters · min^{-1}) (*8*). The crystallization rate was 0.7 mm · hr^{-1} with a rotation rate of 5 rpm. Blue crystals with a very good transparency were pulled from the melt according to the preferential growth *a*-axis up to 50 mm diameter and 70 mm length. Cylinders of 1 cm length and 4 mm diameter were cut along the *a*-axis for EPR and ENDOR measurements.

EPR spectra were recorded on a Bruker 220D spectrometer operating at X-band and equipped with an Oxford Instrument ESR 9 continuous flow helium cryostat. ENDOR experiments were performed using the Bruker ENDOR cavity working in the TM_{110} mode and a 100 W ENI broadband power amplifier. ENDOR spectra were detected using frequency modulation of the rf carrier without magnetic field modulation. The modulation frequency was 12.5 kHz. With this modulation scheme the ENDOR signal has the appearance of the first derivative of the ENDOR enhancement.

III. General Features of EPR and ENDOR Spectra

Figure 2 shows the EPR spectra of a LMA : Ti single crystal recorded at 20 K with the magnetic field **B** parallel and perpendicular to the crystallographic *c*-axis. These spectra have been previously studied and reported separately (*15*). For $\mathbf{B} \| \mathbf{c}$, the spectrum exhibits three lines corresponding to Ti^{3+} ions in three different octahedral sites of the LMA structure. The most populated site, labeled site 3 in Fig. 2, corresponds to the regular octahedral site (2*a*). The two other sites, labeled 1 and 2, correspond, respectively, to the trigonally distorted (4*f*) site and to the low symmetry (12*k*) site. When the magnetic field is perpendicular to the *c*-axis, the EPR line of site 3 is very broad and well separated from the other lines, which essentially belong to site

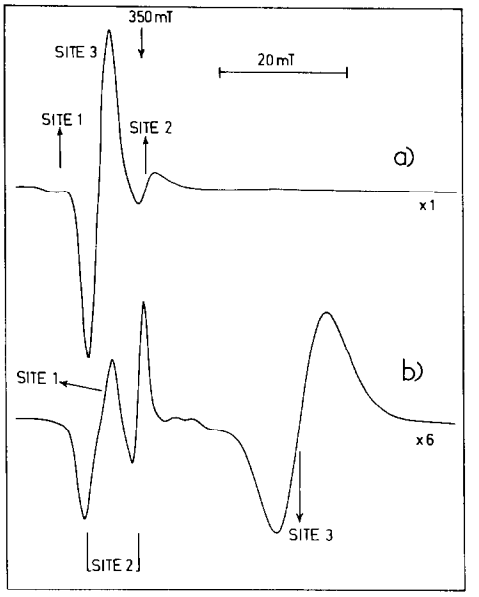

FIG. 2. X-band EPR spectrum at 20 K of a LMA : Ti single crystal. (a) $\mathbf{B} \| \mathbf{c}$. (b) $\mathbf{B} \perp \mathbf{c}$.

2. Only sites 2 and 3 have been identified in ENDOR experiments because their EPR lines are sufficiently intense. The ENDOR lines of site 1 are very weak and always hidden by the ENDOR lines of other sites, so that the present work deals only with Ti^{3+} in (2*a*) and (12*k*) sites.

The ENDOR spectra were studied with the magnetic field **B** perpendicular to the crystallographic axis *a*. An ENDOR spectrum is obtained by partial saturation of an EPR line and by sweeping the radiofrequency radiation through nuclear resonance transitions. Since the EPR lines of sites 2 and 3 occur at different magnetic field values, separate ENDOR spectra of Ti^{3+} in these two sites can thus be obtained.

Figure 3 shows a stack plot representation of the ENDOR spectra recorded with the magnetic field **B** parallel to the crystallographic axis *c*, for different values of the magnetic field B_0 separated by 1 mT. By saturating the EPR spectrum in the magnetic field range of site 3, the ENDOR spectrum is

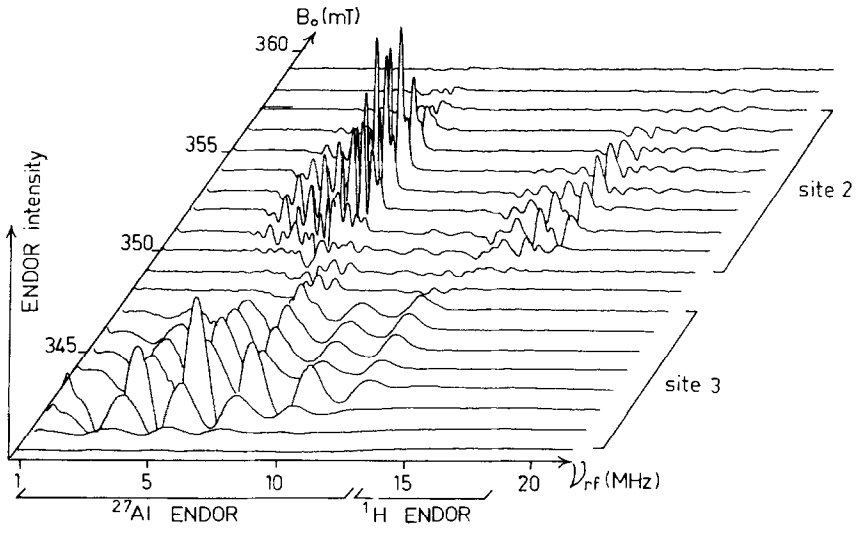

FIG. 3. Stack plot representation of the ENDOR spectra of LMA : Ti recorded at 20 K with $\mathbf{B} \| \mathbf{c}$. Modulation depth 50 kHz. The two horizontal axes represent the radiofrequency ν_{rf} and the magnetic field strength B_0. The broad line spectrum at low magnetic field is due to ^{27}Al nuclei near Ti^{3+} in the (2*a*) site (site 3). The two sets of narrow lines at high magnetic field are due to ^{27}Al nuclei (low frequency) and proton (high frequency) near Ti^{3+} in the (12*k*) site (site 2).

composed of five equally spaced and broad lines, while in the magnetic field range of site 2, it is composed of two sets of relatively narrow lines. The number of ENDOR lines in each set is not well defined and varies with the magnetic field setting. The advantage of the stack plot representation shown in Fig. 3 is to clearly emphasize the differences between the ENDOR spectra of Ti^{3+} in sites 2 and 3. Although these sites are both octahedral with similar cation–oxygen distances and give EPR lines with similar shapes (Fig. 2a), the striking difference in their ENDOR spectra shows that the magnetic interactions of Ti^{3+} with the neighboring atoms are different for the two sites.

The two magnetically abundant nuclei in LMA are ^{27}Al ($I = 5/2$, $Q = 0.15 \times 10^{-28}$ m^2, 100% natural abundance) and ^{139}La ($I = 7/2$, $Q = 0.20 \times 10^{-28}$ m^2, 99.91% natural abundance), where Q is the quadrupole moment. It is thus evident that these two nuclei must be first considered in the interpretation of the ENDOR spectra. In the next two parts we study separately the ENDOR of Ti^{3+} in sites 3 and 2.

IV. ENDOR of Titanium in Site 3

Figure 4 shows the ENDOR spectrum recorded with $\mathbf{B} \| \mathbf{c}$ by setting the magnetic field at the center of EPR line 3 (see Fig. 2a). It is composed of five broad lines with a peak-to-peak width, $\Delta\nu_{pp}$, of about 1 MHz, and of very weak and narrow lines (specified by dashed arrows in Fig. 4). Upon rotation of **B** in the plane perpendicular to **a**, the following modifications of the ENDOR spectrum are observed:

(i) The separation between the broad ENDOR lines decreases when the angle θ from the *c*-axis increases, and the lines nearly collapse at angles of 50° to 60° (Fig. 5b). For these orientations of **B**, one also observes a set of narrow lines with peak-to-peak widths $\Delta\nu_{pp} \approx 0.3$ MHz. These narrow

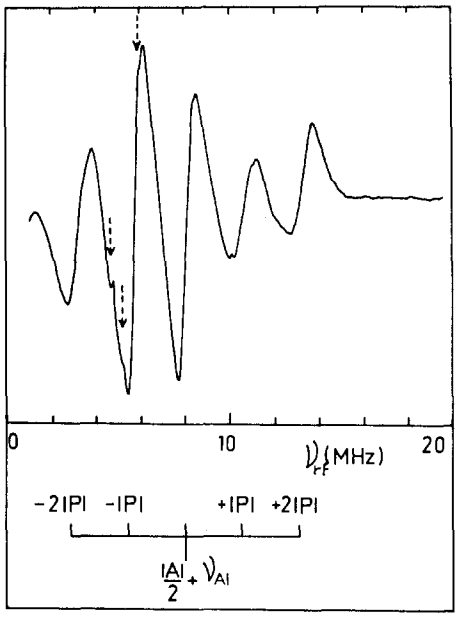

FIG. 4. ^{27}Al ENDOR spectrum of Ti^{3+} in site 3 recorded with $\mathbf{B} \| \mathbf{c}$. Magnetic field setting $B_0 = 345.63$ mT. The dashed arrows represent some of the narrow ENDOR lines superimposed to the broad line ENDOR spectrum.

lines, which are hardly detectable for $\theta = 0°$ (Fig. 4), are now well separated from the other broad lines. These two sets of ENDOR lines correspond to two different kinds of nuclei interacting with Ti^{3+} in site 3.

(ii) A weak ENDOR line is sometimes detectable for **B** at $\theta \approx 10°$ from the c-axis. Its intensity is maximum at $\theta \approx 30°$ (Fig. 5a) and rapidly decreases with increasing θ. It vanishes at θ about 40°. The weakness of this signal and its particular angular variation show that it is not due to the same nuclei which give the two sets of ENDOR lines described in (i). Furthermore it is not observed in all the samples, which definitely indicates that it is not due to the nuclei of the LMA matrix (^{27}Al or ^{139}La). As shown in Section V, this additional line is due to hydrogen impurities. In what follows, we focus exclusively on the intense ENDOR lines which are always observed.

The complexity of the ENDOR spectra shows that they cannot be interpreted using the simple and well-known expression for ENDOR frequencies ν_{rf},

$$\nu_{rf} = |m_s A - g_n \beta_N B_0|, \qquad (1)$$

where A is the hyperfine (hf) interaction and g_n the nuclear g factor. Expression (1) predicts two ENDOR lines, one for each $m_s = \pm\frac{1}{2}$ value. Owing to the fact that both ^{27}Al and ^{139}La nuclei possess a quadrupole moment, we must use a more accurate expression for the ENDOR frequencies.

If we consider the axial symmetry of the (2*a*) site, the spin Hamiltonian describing the interaction of the unpaired electron spin of Ti^{3+} with a single neighboring nuclear spin is given by the expression

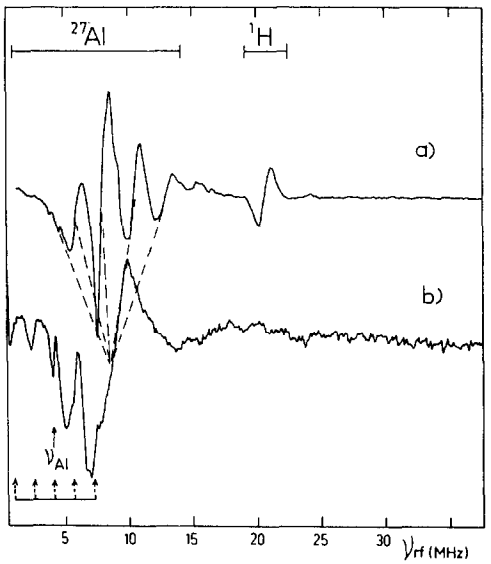

FIG. 5. ^{27}Al ENDOR spectra of Ti^{3+} in site 3, recorded with **B** perpendicular to **a**. (a) **B** at 20° from the c-axis, $B_0 = 348.20$ mT. The isolated line at about 20 MHz is a proton ENDOR line. (b) **B** at 60° from the c-axis, $B_0 = 370.28$ mT. For this magnetic field orientation, the broad ^{27}Al ENDOR lines collapse, which allows the observation of five narrow lines centered at the aluminum nuclear frequency ν_{Al}.

$$H = g\beta B_0 S_z - g_n\beta_N B_0 I_z + A S_z I_z + 0.5P\{I_z^2 - I(I+1)/3\}, \quad (2)$$

where g is given by $g = (g_\parallel^2 \cos^2\theta + g_\perp^2 \sin^2\theta)^{1/2}$ and where A is a nearly isotropic hyperfine interaction and P the quadrupole interaction. In a first-order treatment, the energy levels of the spin states are given by

$$E(m_s, m_I) = g\beta B_0 m_s - g_n\beta_N B_0 m_I + A m_s m_I + 0.5P\{m_I^2 - I(I+1)/3\}. \quad (3)$$

The second-order corrections, which amount to $A^2/2g\beta B_0 \approx 5$ kHz, are much smaller than the linewidth $\Delta\nu_{pp} \approx 1$ MHz and are thus neglected. The ENDOR transitions satisfy the selection rules $\Delta m_s = 0$, $\Delta m_I = \pm 1$ and we thus expect ENDOR lines at frequencies

$$\nu_{rf} = |A m_s - g_n\beta_N B_0 + P(m_I \pm 1/2)|. \quad (4)$$

When the hyperfine structure of the EPR spectrum is resolved, each EPR line is characterized by a single m_I value, which implies that each m_I transition can be saturated individually. In that case either a four-line ENDOR spectrum (for EPR lines $-I < m_I < I$) or only a two-line ENDOR spectrum (for EPR lines $m_I = \pm I$) is observed. Experimentally the hyperfine structure is not resolved in the EPR spectrum of titanium in LMA, and thus several hyperfine lines (characterized by different magnetic quantum numbers m_I) are saturated at each value of the magnetic field. This happens because the resonance condition at a given magnetic field of the EPR line does not define a specific set of nuclear quantum numbers. Moreover if spin diffusion occurs, the EPR line will be saturated over a width much greater than the spin packet width, allowing all the $m_I = 0, \pm 1/2, \ldots, \pm I$ values to be involved in the ENDOR transitions. This is clearly seen in Fig. 3, where the number of ENDOR transitions and their shapes do not depend on the magnetic field setting in the EPR line of site 3.

Since all the m_I values are saturated in the ENDOR experiment, expression (4) indicates that we expect $4 \cdot I = 10$ lines for ^{27}Al nuclei and $4 \cdot I = 14$ lines for ^{139}La nuclei. In addition, this expression shows that the ENDOR frequencies ν_{rf} vary with the magnetic field B_0 and that the curves $\nu_{rf} = f(B_0)$ should be linear with a slope equal to $g_n\beta_N$. It is thus possible to measure the g_n factors and thus to identify the nuclei interacting with the unpaired electron spin of Ti^{3+}. The B_0 dependences of the ENDOR lines of site 3 give $g_n \approx 1.5 \pm 0.2$. This value is close to that of ^{27}Al ($g_{Al} = 1.457$), but does not fit with that of ^{139}La ($g_{La} = 0.795$). We thus conclude that the broad ENDOR lines are due to neighboring Al^{3+} ions, which is not surprising owing to the relatively small Ti^{3+}–Al^{3+} distances compared with the large Ti^{3+}–La^{3+} ones (see Fig. 1).

It should be noticed that each set of ENDOR lines (the broad and the narrow ones) contains only 5 lines instead of the 10 lines expected for ^{27}Al nuclei. Since expression (4) indicates that these 10 lines are decomposed into two m_s sets of 5 lines with $m_s = \pm\frac{1}{2}$, we conclude that we observe only one m_s set of ENDOR transitions. The absence of the other set can be understood by examination of the probabilities $\mathcal{P}$ of dipolar magnetic transition between nuclear spin states, induced by the rf field, which are given in the expression (*20*)

$$\mathcal{P} = k[I(I+1) - m_I(m_I \pm 1)](1 - m_s A/\nu_{Al})^2, \quad (5)$$

where k is a constant. This expression gives the relative intensities of the ENDOR lines and shows that the two m_s sets of transitions should have different intensities. The m_I-dependent term in the right-hand side of expression (5) indicates that the relative intensities in each m_s set are 5:8:9:8:5 and that the m_s-dependent part represents the enhancement factor of the rf field (*20, 21*).

There are two cases where we expect only 5 lines instead of 10: (i) when $A \approx 0$ and (ii) when the condition $m_s A/\nu_{Al} \approx 1$ is satisfied

TABLE II

^{27}Al–ENDOR PARAMETERS IN $LaMgAl_{11}O_{19}:Ti$ FOR THE MAGNETIC FIELD ORIENTATION $B \| c$

Titanium site	Aluminum site	$\|A\|$	$\|P\|$	$\Delta\nu_{pp}$
Site 3 (2*a*)	(12*k*)	8.4 (7)	2.5 (6)	1.0
	Tetrahedral (4*f*)	≈0.0[a]	1.6[a]	0.3[a]
Site 2 (12*k*)	(2*a*)	≈7.7	≈0.4	0.2

Note. $|A|$, $|P|$, and $\Delta\nu_{pp}$ are the hyperfine interaction, the quadrupole interaction, and the peak-to-peak width of the ENDOR lines, respectively. These parameters are given in MH_z.

[a] Values measured with the magnetic field B at 60° from the *c*-axis.

for one of the two m_s values, which gives a zero probability for the corresponding ENDOR transitions. The 5 broad lines shown in Fig. 4 for $\mathbf{B} \| \mathbf{c}$ are located at frequencies $|A|/2 + \nu_{Al} + |P|(m_I \pm \frac{1}{2})$ with $|A| = 8.47$ MHz, $|P| = 2.56$ MHz, and $\nu_{Al} = 3.838$ MHz (Table II). These values give $|m_s A|/\nu_{Al} \approx 1.1$. Consequently, the enhancement factor of the rf field $(1 - m_s A/\nu_{Al})^2$ in expression (5) is equal to 4.41 and 0.01 for the two possible values $m_s = \pm\frac{1}{2}$. We thus expect that the ratio of the intensities of the two m_s sets of ENDOR lines is about 440, so that it is not surprising that we detect 5 lines instead of 10. It should be noted that the relative intensities of the 5 observed lines significantly deviate from the theoretical ratio 5:8:9:8:5. This is because the ENDOR probabilities $\mathcal{P}$ in expression (5) do not take into account the relaxation mechanisms, which are not known in our case.

Figure 6 represents the experimental angular variation of the ENDOR lines of titanium in site 3. The angular variations of the broad ENDOR lines are correctly reproduced using expression (4) with an isotropic hf interaction $|A| = 8.47$ MHz. We estimate that the anisotropy of the hf tensor is less than 0.4 MHz. The quadrupole interaction fits rather well with the expression for axial symmetry $P = P_\parallel(3\cos^2\theta - 1)$ with $|P_\parallel| = 1.28$ MHz and with the axis of the quadrupole interaction parallel to *c*, although it appears evident that there is a small nonaxial component. However, the latter could not be measured because of the considerable broadening of the ENDOR lines when **B** deviates from the *c*-axis.

Let us now consider the narrow ENDOR lines, which can be observed only for magnetic field orientations around $\theta = 60°$, where they are relatively well separated from the broad ENDOR lines because the latter nearly collapse at this angle. Figure 5b shows that these lines (marked by arrows) are centered exactly at the aluminum nuclear frequency ν_{Al}. Thus they are also due to aluminum nuclei, and they occur at frequencies given by expression (4) with $|P'| = 1.6$ MHz and $A' \approx 0$ MHz (Table II). Since a zero hf interaction indicates that there is no electron spin density at the ^{27}Al nuclei, this narrow line ENDOR spectrum can thus be considered as a pure NMR spectrum.

Identification of the Aluminum Nuclei and Crystal Field Disorder

A titanium ion in aluminum site (2*a*) has two different kinds of aluminum neighbors (9), as shown in Fig. 1: the six nearest neighbors at 2.87 Å located in distorted octahedral (12*k*) sites and the six next nearest neighbors at 3.28 Å located in tetrahedral (4*f*) sites. The latter also contain Mg^{2+} ions. ENDOR shows that Ti^{3+} in site 3 exhibits a significant covalent interaction only with one of the two kinds of aluminum neighbors, since only the broad-line ENDOR spectrum is characterized by a large hyperfine parameter $|A| = 8.47$ MHz. The attribution of the high hf interaction to one of the two possible sites is not simple since the hf interaction is almost purely isotropic, and also because contrary to EPR spectroscopy, ENDOR

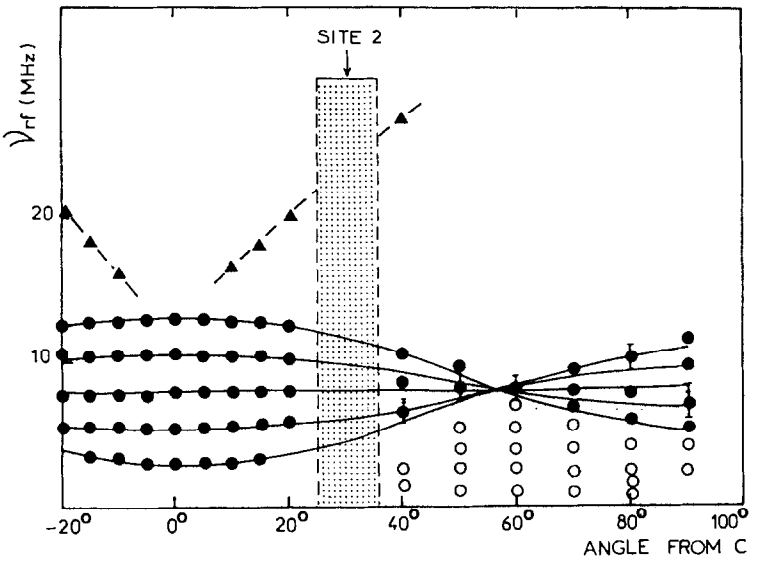

FIG. 6. Angular variation in the plane perpendicular to a of the ENDOR spectrum of Ti^{3+} in the (2*a*) site (site 3). The dashed area represents the angles at which EPR spectra of sites 2 and 3 are superimposed. Triangles: proton ENDOR. Full circles: broad ^{27}Al ENDOR lines due to aluminum in (12*k*) sites. Open circles: narrow ^{27}Al ENDOR lines. The full lines represent calculated angular variations.

spectra do not depend in a simple manner on the number of equivalent nuclei interacting with the unpaired electron spin. It was, however, tempting to assign the high hyperfine coupling $|A| = 8.47$ MHz to interaction with ^{27}Al nuclei in the nearest (12*k*) site because of the short Ti–Al distance in that case.

A quantitative proof for this attribution was obtained from an analysis of the EPR lineshape (Table III). The hf interaction of an unpaired electron spin with N being the equivalent nuclear spin $I = 5/2$ should give $5N + 1$ EPR lines. In the more complicated situation where this hf structure is not resolved, this should result in a contribution ΔB^{hf} to the full width at half amplitude of the EPR absorption given by the expression (*22*)

$$(\Delta B^{hf})^2 = \frac{8 \ln 2}{g^2\beta^2} N(Ah)^2 \frac{I(I+1)}{3}, \quad (6)$$

where A is the aluminum hf interaction measured by ENDOR. $N = 6$ is the number of aluminum ions in the (12*k*) shell, since the latter is almost exclusively occupied by Al^{3+} ions (*9*). Moreover taking into account the mixed occupancy of (4*f*) sites by Al^{3+} and Mg^{2+} ions in equal proportions (*9*), this leads to $N = 3$ for this site. With these two N values, expression (6) gives $\Delta B^{hf} = 3.04$ mT and $\Delta B^{hf} = 2.15$ mT for Al^{3+} ions in (12*k*) sites and (4*f*) sites, respectively.

The true EPR linewidth contains the contribution ΔB^{hf} and a strain-broadening con-

TABLE III

THE RESIDUAL EPR LINEWIDTH ΔB^{hf} AND THE DISTRIBUTION WIDTHS $\sigma g_\parallel$ AND $\sigma\delta$ OF $g_\parallel$ AND OF THE CRYSTAL FIELD SPLITTING δ FOR Ti^{3+} IN THE (2*a*) SITE

ΔB^{hf} (mT)	$g_\parallel$	$\sigma g_\parallel$	δ (cm^{-1})	$\sigma\delta$ (cm^{-1})
3.11	1.9623	1.2×10^{-2}	1200	200
3.04[a]				

[a] Calculated from expression 6 for ^{27}Al nuclei in (12*k*) sites.

tribution, σB, due to the distribution of the resonance field B_0 produced by crystal field disorder. These two kinds of inhomogeneous broadening lead to a Gaussian EPR absorption with full width at half amplitude $\Delta B_{1/2}$, and a first derivative of the absorption with a peak-to-peak linewidth, ΔB_{pp}, given by the expressions (*24*)

$$\Delta B_{1/2} = [(\Delta B^{hf})^2 + (\sigma B)^2]^{1/2}$$
$$\Delta B_{pp} = (2 \ln 2)^{-1/2} \Delta B_{1/2}. \quad (7)$$

ΔB_{pp} was measured experimentally and ΔB^{hf} was calculated for the two possible sites. The strain-broadening contribution σB must thus be determined in order to obtain the experimental value of ΔB^{hf} and to identify the actual aluminum site responsible for the large hf interaction.

A Ti^{3+} ion in the (2*a*) site lies in a crystal field with D_{3d} symmetry, which splits the t_{2g} levels of the *d* orbitals in the purely octahedral field into a_1 and *e* levels separated by the energy δ (Fig. 7). Ti^{3+} thus has a $^2A_1$ ground state characterized by the resonance condition for the EPR line:

$$h\nu = g(\theta)\beta B_0$$
$$\text{with } g(\theta)^2 = g_\parallel^2 \cos^2\theta + g_\perp^2 \sin^2\theta. \quad (8)$$

The $g_\parallel$ and $g_\perp$ factors are given in this case by the expressions (*21*)

$$g_\parallel = (2 + k) \cos 2\gamma - k$$
$$g_\perp = |1 + \cos 2\gamma - \sqrt{2}\, k \sin 2\gamma| \quad (9)$$

with $tg2\gamma = (\lambda\sqrt{2})/(\delta + \lambda/2)$. Experimental results (*15*) give $\delta \approx 1200\ cm^{-1}$. The parameter $k \approx 0.8$ is the orbital reduction factor which takes into account the effect of covalency, and $\lambda = 154\ cm^{-1}$ is the free ion spin–orbit coupling constant.

On the other hand, if a certain amount of crystal field disorder exists, this should modify the energy levels of *d* orbitals from site to site. If the resonance condition and the *g* factor are given by expressions (8) and (9) for one site, a slightly different crystal field at another site will result in a shift, $\Delta\delta$ of the energy splitting of t_{2g} and, through expression (9), in shifts $\Delta g_\parallel$ and $\Delta g_\perp$ of the *g* factor which results in a shift, $\Delta g(\theta)$, of $g(\theta)$ in expression (8),

$$\Delta g(\theta) = (g_\parallel \cos^2\theta\, \Delta g_\parallel + g_\perp \sin^2\theta\, \Delta g_\perp)/g(\theta), \quad (10)$$

which in turn will cause a shift, $\Delta B(\theta)$, of the resonance field B_0 given by

$$\Delta B(\theta) = \frac{h\nu}{\beta} \frac{\Delta g(\theta)}{g(\theta)^2}. \quad (11)$$

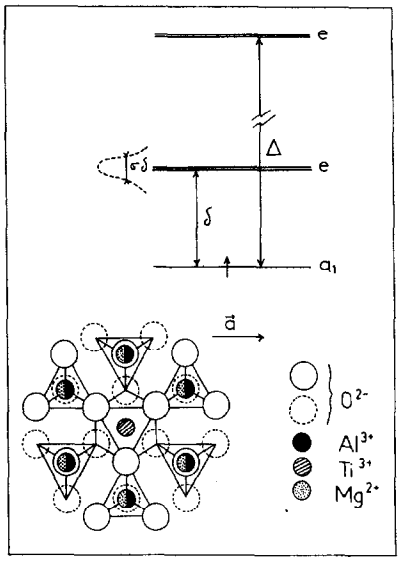

FIG. 7. Splitting of the 3*d* energy levels of titanium in the nearly octahedral crystal field of the (2*a*) site with D_{3d} symmetry. $\Delta \approx 17{,}500\ cm^{-1}$ is the octahedral crystal field measured by Optical absorption (*8*). $\delta \approx 1200\ cm^{-1}$ is the splitting of the t_{2g} level due to the trigonal component of the crystal field, measured by EPR (*15*). $\sigma\delta \approx 200\ cm^{-1}$ is the width of the distribution of the crystal field splitting δ, due to the crystal field disorder at the (2*a*) site. $\sigma\delta$ is obtained from the combination of EPR and ENDOR. This figure also shows the projection in the *ab* plane of the titanium (2*a*) site and the neighboring tetrahedral (4*f*) sites. These sites are occupied either by Al^{3+} or by Mg^{2+} ions in the ratio 1/1. A statistical distribution of these ions in the (4*f*) shell is presumably responsible for the distribution $\sigma\delta$ of the crystal field splitting δ.

It should be noted that $\Delta g_{\parallel}$ and $\Delta g_{\perp}$ are not independent and expressions (9) give the relation $\Delta g_{\perp}/\Delta g_{\parallel} \approx 3$. If we further assume that the distribution of the crystal field splitting δ is Gaussian, this will result in Gaussian distribution of the g factor (24) with a full width at half amplitude $\sigma g(\theta)$, which in turn will give a Gaussian distribution of the resonance field B_0 with a full width at half amplitude $\sigma B(\theta)$ deduced from expression (11),

$$\sigma B(\theta) = \frac{h\nu}{\beta} \frac{\sigma g(\theta)}{g(\theta)^2}, \tag{12}$$

with the corresponding relation $\sigma g_{\perp}/\sigma g_{\parallel} \approx 3$. The resulting peak-to-peak linewidth $\Delta B_{pp}(\theta)$ is deduced from expressions (7) and (12):

$$\Delta B_{pp}(\theta) = (2 \ln 2)^{-1/2} \left[(\Delta B^{hf})^2 + \left(\frac{h\nu}{\beta}\right)^2 \frac{(\sigma g(\theta))^2}{g(\theta)^4} \right]^{1/2}. \tag{13}$$

ΔB^{hf} does not depend on the magnetic field orientation since we know from ENDOR measurements that the aluminum hf interaction A is almost isotropic. Consequently expression (13) gives

$$(\Delta B_{pp})_{\perp}^2 - (\Delta B_{pp})_{\parallel}^2 = (2 \ln 2)^{-1/2} \left(\frac{h\nu}{\beta}\right)^2 \left(\frac{9}{g_{\perp}^4} - \frac{1}{g_{\parallel}^4}\right) (\sigma g_{\parallel})^2. \tag{14}$$

From the experimental values $g_{\parallel} = 1.9623$ and $g_{\perp} = 1.7962$, and from the EPR linewidths $(\Delta B_{pp})_{\parallel} = 3.20$ mT and $(\Delta B_{pp})_{\perp} = 8.00$ mT for $\mathbf{B} \parallel \mathbf{c}$ and $\mathbf{B} \perp \mathbf{c}$, respectively, expressions (14) and (13) give $\sigma g_{\parallel} = 1.2 \times 10^{-2}$ and $\Delta B^{hf} = 3.11$ mT. The latter value is close to $\Delta B^{hf} = 3.04$ mT and significantly different from $\Delta B_{hf} = 2.15$ mT previously calculated for an unresolved hf interaction with aluminum nuclei in (12k) and (4f) sites, respectively.

We may thus conclude that the strong titanium–aluminum hf interaction occurs exclusively with aluminum nuclei in the nearest (12k) sites. There is no hf interaction with aluminum nuclei in the next nearest (4f) sites, which are presumably responsible of the narrow ^{27}Al ENDOR lines characterized by $A \approx 0$ MHz.

Moreover, the important widths $\sigma g_{\parallel} = 1.2 \times 10^{-2}$ and $\sigma g_{\perp} = 3.6 \times 10^{-2}$ of the g tensor distribution show that Ti^{3+} in the (2a) site experiences an important crystal field disorder, which seems fairly general in these types of hexaaluminates (23). We may estimate the distribution width $\sigma\delta$ of the crystal field splitting δ around the mean value $\delta \approx 1200$ cm^{-1} (Fig. 7). The slopes of the curves $g_{\parallel} = f(\delta)$ and $g_{\perp} = f(\delta)$ given in expressions (9) yield $\sigma\delta \approx 200$ cm^{-1}.

This very important strain broadening of the electronic energy levels should perturb the optical properties of the material. In particular, it could likely be at the origin of the important broadening of the zero phonon transition that was observed for the $^2E \rightarrow {}^2T_2$ emission of Ti^{3+} in the (2a) site (15). This crystal field disorder at the (2a) site could originate from a disorder in the next nearest cationic (4f) shell, which is occupied by Al^{3+} and Mg^{2+} ions in the ratio 1/1 for the stoichiometric composition $LaMgAl_{11}O_{19}$. A schematic representation of Ti^{3+} in the (2a) site surrounded by the six tetrahedral (4f) sites is shown in Fig. 7. Owing to the mixed occupancy of these sites by Al^{3+} and Mg^{2+}, the (2a) site can assume a symmetry lower than D_{3d}, which varies from site to site depending on the exact Al/Mg configuration in the (4f) shell. Taking into account the important difference between the ionic radii of Al^{3+} (0.53 Å) and Mg^{2+} (0.71 Å) (25), a significant strain should result from the existence of many different cationic configurations in the (4f) shell surrounding Ti^{3+} in the (2a) site.

Hyperfine Parameters

The titanium (2a)–aluminum (12k) hyperfine interaction is normally composed of an

isotropic A_s and an anisotropic term A_p according to the relation

$$A(\alpha) = A_s + A_p(3\cos^2\alpha - 1), \quad (15)$$

where α is the angle between **B** and the titanium–aluminum direction. Experimentally, the very small anisotropy of $|A|$, less than 0.4 MHz, implies that $|A_p|$ is less than 0.13 MHz. A_s arises from the presence of unpaired electrons in s orbitals of Al^{3+} due to covalent bonding. A_p is the sum of a point dipole–dipole interaction A_d, between the ^{27}Al nucleus and the unpaired electron spin of Ti^{3+}, and A_σ and A_π interactions arising from the presence of unpaired electrons in p_σ and p_π orbitals of Al^{3+} due to covalent bonding. The total anisotropic interaction A_p is given by (*26*)

$$A_p = A_d + A_\sigma - A_\pi \quad \text{with } A_d = g\beta g_{Al}\beta_N R^{-3}. \quad (16)$$

From the Ti^{3+}–Al^{3+} distance $R = 2.87$ Å (*9*), we obtain $A_d = +0.87$ MHz. The existence of a negative contribution, $A_\sigma - A_\pi$, of covalent bonding, which amounts to -0.7 or -1.0 MHz depending on the sign of A_p, could explain the quasi-isotropy of the hf interaction. The largest contribution to the hf interaction is due to the isotropic term A_s which amounts to $|A_s| \approx 8.2$ or 8.7 MHz, depending on the sign of A_p.

The spin transfer in aluminum s orbitals occurs either via a Ti^{3+}–O^{2-}–Al^{3+} bond, as with cation–cation interactions in other aluminates (*27*), or via a direct $Ti^{3+}\rightarrow Al^{3+}$ interaction. In the first case, we expect a small and negative spin density (*27*) at the aluminum s orbital originating from a polarized transfer of unpaired spin from filled oxygen p orbitals to empty (antibonding) e orbitals of titanium, i.e., $A_s < 0$. In LMA, the isotropic hf interaction is, however, significantly higher than the value $A_s = -1.11$ MHz measured for Cr^{3+}–Al^{3+} interactions in $LaAlO_3$, which occurs by the same mechanism (*27*). Alternatively, a small amount of direct $Ti^{3+}\rightarrow Al^{3+}$ spin transfer should result in a positive spin density (*26*) at ^{27}Al nuclei, i.e., $A_s > 0$. Unfortunately we could not measure the sign of the hf interaction, so that it was not possible to determine the origin of the large covalent interaction between Ti^{3+} and Al^{3+} in (12*k*) sites.

The quadrupole interaction $P_\parallel$ is related to the electric field gradient q at the ^{27}Al nucleus and to its quadrupole moment Q by the expression:

$$P_\parallel = (3e^2Qq)/(4I(2I - 1) \quad \text{with } eq = \partial E_z/\partial z. \quad (17)$$

The experimental quadrupole interaction $|P_\parallel| = 1.28$ MHz gives the value $|q| = 2.94 \times 10^{40}$ V m^{-2} C^{-1} for the electric field gradient q at the aluminum nucleus in the (12*k*) site.

V. ENDOR of Titanium in Site 2

Figure 2 shows the EPR line of Ti^{3+} in site 2 for two orientations of the magnetic field **B** with respect to the crystallographic axis c. The g tensor (Table I) indicates that this site corresponds to the octahedral (12*k*) site of the spinel blocks (Fig. 1). Despite the low EPR intensity, we obtained a strong and well-characterized ENDOR spectrum for site 2 because the corresponding EPR line is always well separated from that of site 3, and also because the ENDOR lines are much narrower than those of site 3.

The general ENDOR features of site 2 are clearly emphasized in the stack plot representation of Fig. 3. For this magnetic field orientation (**B** $\parallel$ **c**), the spectra are composed of two sets of relatively narrow ENDOR lines located at different frequencies of the rf field. The first one, which occurs in the frequency range 4.0 to 8.5 MHz, is composed of 10 to 12 narrow lines (linewidth $\Delta\nu_{pp} \approx 0.2$ MHz), while the other set (linewidth $\Delta\nu_{pp} \approx 0.4$ to 0.5 MHz), which lies in the frequency range 15 to 20 MHz, is composed of one pronounced line sur-

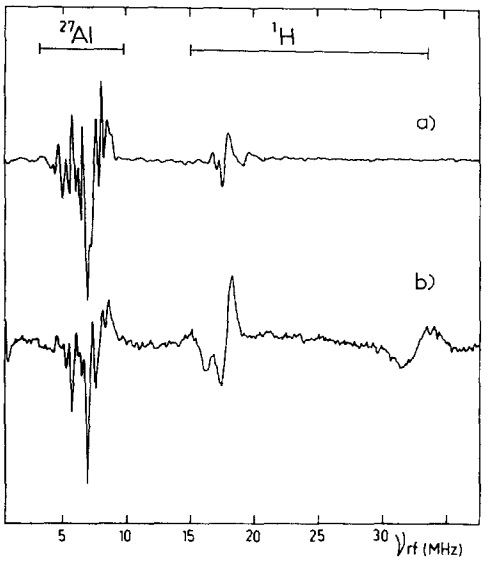

FIG. 8. Two representative ENDOR spectra of Ti^{3+} in the (12*k*) site (site 2) showing ^{27}Al and ^{1}H ENDOR lines. (a) $\mathbf{B} \| \mathbf{c}$; magnetic field setting $B_0 = 353.85$ mT. (b) $\mathbf{B} \perp \mathbf{a}$, at 50° from the *c*-axis; magnetic field setting $B_0 = 347.98$ mT.

rounded by two or three weaker lines. The number of apparent lines in each set is not well defined and varies with the magnetic field setting B_0. Figure 8a shows an example of an ENDOR spectrum for the orientation $\mathbf{B} \| \mathbf{c}$, recorded by setting the magnetic field at the center of the EPR line ($B_0 = 353.85$ mT).

Upon deviation of the magnetic field **B** from the *c*-axis, there is no shift of the low-frequency ENDOR lines. However, the number of lines and their relative intensities vary with the orientation of **B** (Fig. 8b), so that it was not possible to follow the angular variation of each line. Consequently, their angular variation is only represented by a shaded area in Fig. 9. In contrast, there is a dramatic modification of the high-frequency part of the spectrum when **B** deviates from the *c*-axis. The first modification is a rapid broadening of the less intense lines and their progressive disappearance. The strongest line splits into three lines, and one of them migrates toward high frequency upon increasing the angle θ between **B** and the *c*-axis (Figs. 8b and 9). This shift is accompanied by a line broadening, so that the amplitude decreases, and the line is no longer detectable when the angle θ between **B** and the *c*-axis is larger than 60°. The two other lines exhibit only a small shift toward low frequencies and merge into one line for θ larger than about 60°. The resulting angular variation of all the ENDOR lines of Ti^{3+} in site 2 is shown in Fig. 9.

Owing to the position of the (12*k*) site with respect to the mirror plane containing La^{3+} ions, the question to be addressed is that of the identification of the nuclei interacting with the unpaired electron spin. The different behaviors of the two sets of ENDOR lines show that they belong to different nuclei. The first evidence comes from the lack of quadrupolar splitting of the lines at high frequency, which indicates that they belong to the nuclear spin $I = \frac{1}{2}$. Such nuclear spin does not normally exist in LMA. On the other hand, the low-frequency set of ENDOR lines exhibits a pronounced quadrupolar splitting, which is normal behavior for ^{27}Al or ^{139}La nuclei with nuclear spins $I = \frac{5}{2}$ and $I = \frac{7}{2}$, respectively. The identification of the nuclei is possible from the magnetic field dependence of the ENDOR frequencies for $\mathbf{B} \| \mathbf{c}$ (Fig. 3). From plots of the resonance frequency ν_{rf} with respect to the magnetic field strength B_0 (expressions (1) and (4)), we obtain $g_n \approx 1.7 \pm 0.3$ for the ENDOR lines at low frequencies and $g_n \approx 5.9 \pm 0.6$ for the ENDOR lines at low and high frequencies, respectively. The former value is close to the nuclear *g* factor of ^{27}Al ($g_{Al} = 1.457$) and significantly higher than that of ^{139}La ($g_{La} = 0.795$). Consequently, we attribute the narrow lines at low frequency to ^{27}Al ENDOR. The other experimental g_n value measured for the high-frequency ENDOR lines is close to the nuclear *g* factor of the proton ($g_H = 5.586$, $I = \frac{1}{2}$)

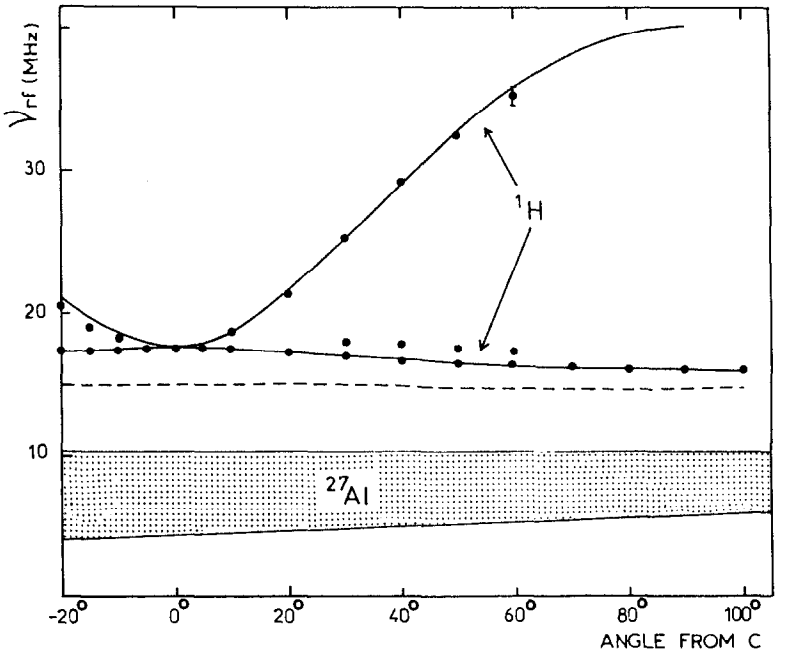

FIG. 9. Angular variation of ENDOR of Ti^{3+} in the (12*k*) site (site 2), in the plane perpendicular to the *a* direction. Circles: experimental points. Full lines: calculated angular variation. Dotted line: variation of the proton nuclear frequency. The shaded area represents the frequency domain of ^{27}Al ENDOR lines.

and ^{19}F (g_F = 5.258, $I = \frac{1}{2}$, 100% abundance). Since there is no objective reason for an accidental diffusion of fluorine in the LMA crystals and owing to the well-documented evidence of hydrogen diffusion in the spinel $MgAl_2O_4$ (*19*), we attribute these ENDOR lines to protons trapped near Ti^{3+} ions in (12*k*) sites.

For the same reasons, we also attribute to proton ENDOR the high-frequency line sometimes observed in spectra of Ti^{3+} in site 3 (see Section IV and Figs. 5a and 6) because it takes the same g_n value as the proton ENDOR lines of site 2. However, this proton line is often absent or very weak in the case of site 3. In contrast, proton lines are always present in the case of site 2, and their intensity is high, especially when **B** is not parallel to the *c*-axis. Consequently, a large fraction of Ti^{3+} in site 2, if not all, possesses a neighboring proton defect. This agrees with the previous EPR investigation which suggested that this Ti^{3+} ion is adjacent to a cationic defect (*15*).

It should be noted that the ENDOR lines shown in Fig. 8, which were recorded by setting B_0 at the center of the EPR line, correspond only to one m_s state, although Eq. (1), which applies for proton ENDOR, predicts one line for each $m_s = \pm\frac{1}{2}$ state. However, the missing lines are observed at low frequencies, although very weak, at high amplification, or when B_0 is set at the low field flank of the EPR line (see, for example, Fig. 3 for B_0 = 349 to 352 mT). Such phenomena, i.e., the observation of only one m_s state for a given field setting, have already been observed when the nuclear

spin lattice relaxation time T_{1n} is much longer than the electron spin lattice relaxation time T_{1e} (*28*).

Identification of the Proton Defect

We have measured the principal values A_i ($i = 1, 2, 3$) of the proton hf interaction from the angular variation of the ENDOR lines (Fig. 9), which allowed us to deduce the localization of the proton site with respect to that of the Ti^{3+} ion. Taking into account the small anisotropy of the EPR line in the plane perpendicular to **a** (Table I), the g factor can be neglected in the calculation of ENDOR frequencies, which are given by the following expression for an arbitrary orientation of **B**,

$$\nu_{rf} = \left[\sum_{i=1}^{3} h_i^2 (m_s A_i - \nu_H)^2\right]^{1/2}, \quad (18)$$

where h_i is the direction cosine between **B** and the i^{th} hyperfine tensor axis. The fact that the lines nearly collapse when **B** is parallel to the c-axis indicates that all the Ti^{3+}–proton pairs are equivalent for this orientation and that the Ti^{3+}–proton directions are perpendicular to the c-axis. This orientation corresponds to $h_1 = 1, h_2 = h_3 = 0$ and expression (18) is thus reduced to $\nu(m_s) = |m_s A_1 - \nu_H|$. The existence of a maximum of three lines in the angular variation shows that there is no site splitting, which implies that the two other components of the hf interaction are parallel to two crystallographic axes in the basal plane ab. The solid lines in Fig. 9 represent the angular variations calculated using the following hf parameters: $A_3 = +61.2$ MHz, $A_2 = +5.07$ MHz, and $A_1 = +2.64$ MHz. The A_3 axis is parallel to the a-axis, which indicates that the Ti^{3+}–proton pair is oriented along a (12*k*)–(12*k*) direction.

The isotropic component A_s of the proton hf interaction is found to be equal to $A_s = (A_1 + A_2 + A_3)/3 = +23.0$ MHz, which gives a spin density at the proton equal to $\rho_H = +16.2 \times 10^{-3}$. The most important term for the estimation of the titanium–proton distance is the anisotropic part of the hf interaction. Normally, if this contribution is a purely point dipole–dipole interaction, A_d, we expect an axial A tensor with $A_3 = A_s + 2A_d$ and $A_d = g\beta g_n \beta_N R^{-3}$. However, the small anisotropy $A_2 - A_1 = 2.43$ MHz measured in the present case indicates that in addition to A_d, there is a small contribution of a finite spin density in p orbitals of the oxygen ions forming the OH bond. If this contribution is neglected, A_d is estimated to be $A_d = +19.1$ MHz, which gives $R \approx 1.6$ Å for the titanium–proton distance. It should be noted that this distance is approximately half the distance 2.80 Å between two adjacent (12*k*) sites, which strongly suggests that the proton is trapped at an interstitial position between the two O^{2-} ions sharing two (12*k*) sites, forming a $(OHO)^{3-}$ complex as in the cases of YAG (*30*) and α-Al_2O_3 (*31*).

The structure proposed for the Ti^{3+}–H^+ pair is shown in Fig. 10. It should be emphasized that the proton is exclusively localized between two adjacent (12*k*) sites, although there are many possible configurations for the $(OHO)^{3-}$ complex around the (12*k*) site. The existence of a specific localization for the proton suggests that it acts as a charge compensator for a cationic defect in the (12*k*) site adjacent to Ti^{3+}. This defect is most probably a Mg^{2+} ion substituting an Al^{3+} ion. In LMA, the normal site of Mg^{2+} is the tetrahedral (4*f*) site (*9*), but an antisite disorder involving a small amount of interchange of Mg^{2+} and Al^{3+} between (4*f*) and (12*k*) sites appears very likely, as in the case of the spinel $MgAl_2O_4$. Substitution of an Al^{3+} in the (12*k*) site by a Mg^{2+} ion induces a local excess of negative charge which can be compensated by a defect with positive charge (*32*). We thus propose that the titanium center previously labeled Ti^{3+} (site 2) is a neutral Ti^{3+} (H^+, Mg^{2+}) defect cluster,

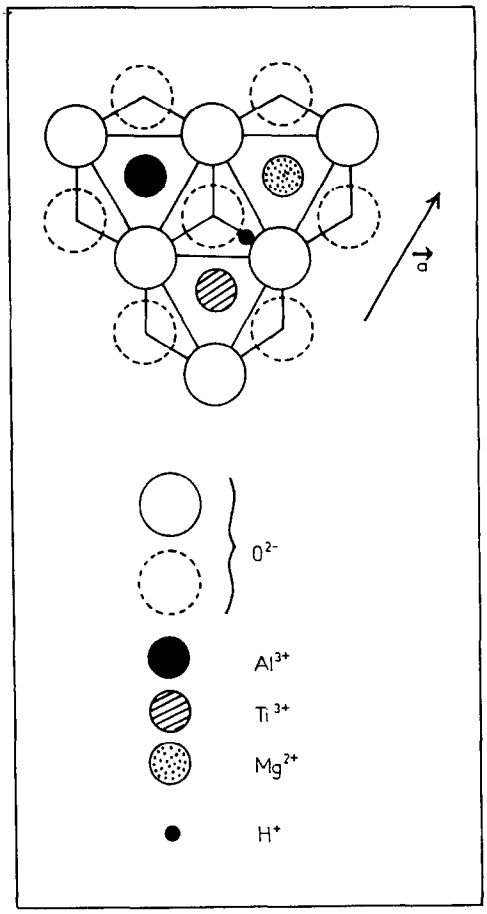

FIG. 10. Proposed model for the Ti^{3+} (site 2) defect cluster. This defect is a $(Ti_{Al}{}^{x}H_i^{\cdot} \cdot Mg_{Al}{}')$ cluster formed by a Ti^{3+} ion in the (12*k*) position, adjacent to a Mg^{2+} ion in a neighboring (12*k*) site. The proton is trapped at the interstitial position between the two bridging O^{2-} ions, forming a $(OHO)^{3-}$ complex.

denoted $(Ti_{Al}{}^{x}H_i^{\cdot} \cdot Mg_{Al}{}')$ in Kroger–Vink notation. EPR intensity measurements show that the concentration of this titanium center is about $2 \times 10^{18}\,cm^{-3}$ for the composition $x = 0.1$. This value also gives the lowest limit for the proton concentration in LMA.

Aluminum hf Interaction

Because of the complicated pattern shown by the ^{27}Al ENDOR lines of site 2 (Fig. 8), we could not derive precise hf parameters. However, the center of gravity of the aluminum ENDOR lines occurs at about the same frequency for site 2 and site 3 (Fig. 3). The existence of a complex spectrum for site 2 indicates that the unpaired electron spin interacts with slightly nonequivalent aluminum nuclei. If we compare the aluminum ENDOR spectra of Ti^{3+} in these two sites (Fig. 3), it appears that the differences arise from the linewidths and the quadrupole splitting of ENDOR lines, which are smaller for site 2. Applying Eq. (4) for the ^{27}Al ENDOR lines recorded with $\mathbf{B} \| \mathbf{c}$ (Figs. 3 and 8a), the parameters $|A| \approx 7.7$ MHz and $|P| \approx 0.4$ MHz are obtained (Table II).

The neighboring aluminum sites which can give hf interactions with Ti^{3+} in the (12*k*) site are one (12*k*) site at 2.78 Å, one (2*a*) site at 2.87 Å, three tetrahedral (4*f*) sites at 3.30 Å, and two octahedral (4*f*) sites at 3.32 Å. The existence of a very small quadrupole interaction, $|P_{\|}| \approx |P|/2 \approx 0.2$ MHz, indicates that the site of the ^{27}Al nucleus is not distorted, which is the case for the (2*a*) and the tetrahedral (4*f*) sites. Owing to the smaller (12*k*)–(2*a*) distance and to the previous evidence of a strong Ti^{3+} (2*a*)–Al^{3+} (12*k*) interaction (see Part IV), we attribute the ^{27}Al ENDOR lines of site 2 to Ti^{3+} (12*k*)–Al^{3+} (2*a*) interactions.

VI. Conclusion

Crystals of $LaMgAl_{11}O_{19}$ doped with Ti^{3+} were studied by electron nuclear double resonance spectroscopy. Among the three octahedral sites occupied by titanium, only the most populated (2*a*) and (12*k*) sites have been identified in the ENDOR experiments.

ENDOR of ^{27}Al nuclei showed that there is an important covalent interaction between Ti^{3+} and Al^{3+} ions in (2*a*) and (12*k*) sites of the spinel blocks. In addition, an important crystal field disorder prevails for Ti^{3+} in the (2*a*) site, presumably due to a statistical occupation of the neighboring tet-

rahedral (4*f*) sites by Mg^{2+} and Al^{3+} ions. It was also shown that a proton impurity is trapped near Ti^{3+} in octahedral (12*k*) sites. This proton is localized between two oxygen ions sharing two (12*k*) sites, forming a $(OHO)^{3-}$ complex. A defect model in which the protons act as charge compensators for Mg^{2+} ions substituting Al^{3+} ions in (12*k*) sites adjacent to the Ti^{3+} ions is proposed. This neutral species is described as a $(Ti_{Al}^{x}H_i^{\cdot}\ Mg_{Al}')$ cluster.

References

1. W. R. Rapoport and C. P. Khattak, *Appl. Opt.* **27,** 2677 (1988).
2. G. T. Forrest, *Laser Focus World* **25,** 23 (1989).
3. W. Strek, P. Deren, and B. Jezowska-Trzebiatowska, *J. Phys. C* **48**(7), 455 (1987).
4. J. Kvapil, M. Koselja, J. Kvapil, P. Pernel, V. Skoda, J. Kubelka, K. Hamal, and K. Kubecek, *Czech. J. Phys. B* **38,** 237 (1988).
5. P. Peshev, V. Petrov, and N. Manuilov, *Mater. Res. Bull.* **23,** 1193 (1988).
6. Y. Segana, A. Sugimoto, P. H. Kim, S. Namba, K. Yamagishi, Y. Anzai, and Y. Yamagushi, *Jpn. J. Appl. Phys.* **26,** L291 (1987).
7. A. I. Alimpiev, G. V. Bukin, V. N. Matrosov, E. V. Pestriakov, V. P. Solntsev, V. J. Trunov, E. G. Tsvetkov, and V. P. Chebotaev, *Sov. J. Quantum Electron.* **16**(5), 579 (1986).
8. C. Wyon, J. J. Aubert, D. Vivien, A. M. Lejus, and R. Moncorge, *J. Lumin.* **40**(1), 871 (1988).
9. M. Gasperin, M. C. Saine, A. Kahn, F. Laville, and A. M. Lejus, *J. Solid State Chem.* **54,** 61 (1984).
10. A. Kahn, A. M. Lejus, M. Madsac, J. Thery, D. Vivien, and J. C. Bernier, *J. Appl. Phys.* **52,** 11 (1981); M. I. Demchouk, A. K. Gilev, A. M. Zabaznov, V. P. Mikhailov, A. A. Stratov, and A. P. Shkadarevitch, *Opt. Commun.* **55,** 207 (1985).
11. F. Laville, M. Perrin, A. M. Lejus, M. Gasperin, R. Moncorge, and D. Vivien, *J. Solid State Chem.* **65,** 301 (1986); R. Moncorge, T. Benyahou, D. Vivien, and A. M. Lejus, *J. Lumin.* **35,** 199 (1986).
12. B. Viana, A. M. Lejus, D. Vivien, V. Poncon, and J. Boulon, *J. Solid State Chem.* **71,** 77 (1987).
13. J. Xiaobo, J. Yandao, L. Jingkui, X. Hongchang, and C. Yinping, *J. Cryst. Growth* **97,** 761 (1989).
14. B. Martinat, A. M. Lejus, and D. Vivien, *Mater. Res. Bull.* **25,** 523 (1990).
15. D. Gourier, L. Colle, A. M. Lejus, D. Vivien, and R. Moncorge, *J. Appl. Phys.* **63,** 1144 (1988).
16. B. Martinat, D. Gourier, A. M. Lejus, and D. Vivien, *J. Solid State Chem.* **89,** 147 (1990).
17. C. Borel, C. Wyon, and J. J. Aubert, private communication.
18. G. Feher, *Phys. Rev.* **103,** 834 (1956).
19. R. Gonzalez, Y. Chen, J. F. Barhorst, and K. L. Tsang, *J. Mater. Res.* **2,** 77 (1987).
20. D. H. Whiffen, *Mol. Phys.* **10,** 595 (1966); N. M. Atherton, *in* "Electron Spin Resonance," Wiley, London (1973).
21. A. Abragam and B. Bleaney, *in* "Electron Paramagnetic Resonance of Transition Metal Ions," Oxford Univ. Press (Clarendon), Oxford (1971).
22. H. Seidel and H. C. Wolf, *in* "Physics of Color Centres" (W. Fowler, Ed.), p. 557, Academic Press, New York (1968).
23. D. Gourier, D. Vivien, J. Thery, J. Livage, and R. Collongues, *Phys. Status Solidi A* **45,** 599 (1978).
24. W. Froncisz and J. S. Hyde, *J. Chem. Phys.* **73,** 3123 (1980).
25. R. D. Shannon and C. T. Prewitt, *Acta Crystallogr. Sect. B* **25,** 925 (1969).
26. J. Owen and J. H. Thornley, *Rep. Prog. Phys.* **29,** 675 (1966).
27. D. R. Taylor, J. Owen, and B. M. Wanklyn, *J. Phys. C* **6,** 2592 (1973).
28. L. Kevan and L. D. Kispert, *in* "Electron Spin Double Resonance Spectroscopy," p. 21, Wiley, London (1976).
29. T. G. Brown and B. M. Hoffman, *Mol. Phys.* **39,** 1073 (1980).
30. D. P. Devor, R. C. Pastor, and L. G. Deshazer, *J. Chem. Phys.* **81,** 4104 (1984).
31. P. Balmer, H. Blum, M. Forster, A. Schweiger, and H. Gunthardt, *J. Phys. C* **13,** 517 (1980).
32. G. S. White, R. V. Jones, and J. H. Crawford, *J. Appl. Phys.* **53,** 265 (1982).